Noname manuscript No.
(will be inserted by the editor)

Influence of Vessel Curvature and Plaque Composition on Drug Transport in the Arterial Wall following Drug-eluting Stent Implantation

Javier Escuer · Irene Aznar · Christopher McCormick · Estefanía Peña · Sean McGinty · Miguel A. Martínez

Received: date / Accepted: date

Abstract In the last decade, many computational models have been developed to describe the transport of drug eluted from stents and the subsequent uptake into arterial tissue. Each of these models has its own set of limitations: for example, models typically employ simplified stent and arterial geometries, some models assume a homogeneous arterial wall, and others neglect the influence of blood flow and plasma filtration on the drug transport process. In this study, we focus on two common limitations. Specifically, we provide a comprehensive investigation of the influence of arterial curvature and plaque composition on drug transport in the arterial wall following drug-eluting stent implantation. The arterial wall is considered as a three-layer structure including the subendothelial space, the media and the adventitia, with porous membranes separating them (endothelium, internal elastic and external lamina). Blood flow is modelled by the Navier-Stokes equations while Darcy's law is used to calculate plasma filtration through the porous layers. Our findings demonstrate that arterial curvature and plaque composition have important influences on the spatio-temporal distribution of drug, with potential implications in terms of effectiveness of the treatment. Since the majority of computational models tend to neglect these features, these models are likely to be under- or over-estimating drug uptake and redistribution in arterial tissue.

Keywords Drug transport · Drug-eluting stents · Arterial wall · Curvature · Atheroma plaque

J. Escuer
Aragón Institute for Engineering Research (I3A), University of Zaragoza, Spain.

I. Aznar
Aragón Institute for Engineering Research (I3A), University of Zaragoza, Spain.

C. McCormick
Department of Biomedical Engineering, University of Strathclyde, Glasgow, UK.

E. Peña
Aragón Institute for Engineering Research (I3A), University of Zaragoza, Spain.
Biomedical Research Networking Center in Bioengineering, Biomaterials and Nanomedicine (CIBER-BBN), Spain.

S. McGinty
Division of Biomedical Engineering, University of Glasgow, Glasgow, UK.

M. A. Martínez
Aragón Institute for Engineering Research (I3A), University of Zaragoza, Spain.
Biomedical Research Networking Center in Bioengineering, Biomaterials and Nanomedicine (CIBER-BBN), Spain.
María de Luna, 3. E-50018 Zaragoza (Spain).
E-mail: miguelam@unizar.es

1 Introduction

Coronary artery disease (CAD) is the leading cause of death globally [Roth et al., 2018]. Atherosclerosis is the major contributor of CAD and results from the abnormal accumulation of fat, cholesterol, macrophages, calcium and other substances inside the vessel, leading to the partial or total reduction of the blood flow through the coronary arteries to the heart muscle.

Coronary angioplasty with stenting has revolutionized the treatment of advanced atherosclerotic lesions in arteries. However, in-stent restenosis (ISR), a gradual luminal re-narrowing mainly due to the response to vessel wall injury induced by the device, is the major clinical limitation of this technique [Alfonso et al., 2014]. The advent of drug-eluting stents (DES), which release antiproliferative substances into the arterial tissue, and

improved stent designs, have contributed to substantially reduce the occurrence of ISR compared with bare metal stents (BMS). However, ISR still remains a significant clinical and technological challenge. Moreover, an increased risk of developing late or very-late stent thrombosis (LST/VLST) following DES implantation, which has been associated with high rates of mortality, has emerged as a major safety concern [Alfonso et al., 2014; Byrne et al., 2015].

Computational modelling and numerical simulation have risen as a fundamental tool in the investigation of medical devices, helping to address some of the limitations of often difficult, expensive and extremely variable experimental/clinical tests. In the particular case of DES, computational analysis has enhanced the understanding of the factors which govern drug release from the device and drug binding and redistribution within the arterial wall. Such efforts are helping in the development of a safer and more effective new generation of DES.

In the last decade, a large number of computational studies have been developed to describe the transport of drug eluted from stents in arteries (e.g. Vairo et al. [2010]; McGinty et al. [2010]; Tzafriri et al. [2012]; Bozsak et al. [2014]; McGinty and Pontrelli [2015, 2016]; Ferreira et al. [2017, 2018]; Mandal and Mandal [2018]; McKittrick et al. [2019]). These models generally consider a healthy straight vessel geometry with diffusive, advective and binding processes governing the transport of the drug within the blood flow and through the respective porous layers of the arterial wall. However, such models do not take into account the considerable geometric variability of the coronary artery (curved regions, branching, etc.) which is associated with alterations in the local hemodynamics, playing an important role in the localization of the atherosclerotic lesions [Frangos et al., 1999; Tarbell, 2003]. The influence of coronary arterial curvature on mass transport has previously been investigated for other macromolecules such as low-density lipoproteins (LDL), showing different average concentrations of LDL in curved arteries compared with straight arteries [Caputo et al., 2013; Wang and Vafai, 2015]. However, to the best of our knowledge, in terms of drug transport there are only a very limited number of computational approaches available in the literature that take into account complex arterial geometries [Hossain et al., 2012; Cutrì et al., 2013], but they are not specifically focussed on the effect of the curvature of the vessel on tissue uptake and retention of drug.

Moreover, there is growing evidence that plaque composition may well have an impact on drug distribution within diseased tissue [McKittrick et al., 2016]. However, very few of the computational models of drug transport in arteries from the available literature incorporate the existence of disease state [Vairo et al., 2010; McGinty et al., 2010; Hossain et al., 2012; Ferreira et al., 2017, 2018; Mandal and Mandal, 2018]. Of the models that do, for instance, Vairo et al. [2010] assume a porous homogeneous plaque between the device and the healthy tissue in their 2D-axisymmetric geometry, but the process of binding is described in terms of equilibrium conditions. Hossain et al. [2012] perform several simulations on a 3D patient-specific geometry of a bifurcation of a two-layered coronary artery with a plaque in order to analyse the effect of both artery and plaque heterogeneity on drug transport. However, a first order reaction kinetics model was adopted to account for possible drug binding. Mandal and Mandal [2018] also present a 2D-axisymmetric model and take into consideration the binding and unbinding processes to describe the interaction of the drug with the healthy and unhealthy tissue, but the porous nature of the arterial wall is not fully taken into account. Finally, Ferreira et al. use different 2D geometries to investigate the impact of local plaque composition [Ferreira et al., 2017] and plaque eccentricity on drug distribution [Ferreira et al., 2018] but, like most other drug transport models [Vairo et al., 2010; Tzafriri et al., 2012; Cutrì et al., 2013; McGinty and Pontrelli, 2015, 2016; Ferreira et al., 2017; Mandal and Mandal, 2018; Ferreira et al., 2018; McKittrick et al., 2019] the arterial wall is modelled as a single layer, limiting the interpretation of the results.

In this work, we provide a comprehensive computational study of the impact of the variability of the coronary artery geometry on drug transport in the blood flow and in the arterial wall. In particular, we perform a series of simulations to elucidate the effect of arterial curvature on spatio-temporal drug uptake within tissue. Computations are also carried out on an idealised curved coronary artery geometry under diseased conditions, simulated by the presence of an atherosclerotic plaque between DES and tissue, and the effect of the plaque heterogeneity on the overall drug distribution is investigated. Our model incorporates the generally accepted nonlinear saturable reversible binding model [Tzafriri et al., 2012; McGinty and Pontrelli, 2016; McKittrick et al., 2019] to describe the reversible reaction of the free drug molecules (ligands).

The paper is organised as follows. We start with a description of how we model blood flow in the lumen (Section 2.1.1), followed by plasma filtration through the tissue (Section 2.1.2). We then present equations to describe drug release from the stent and subsequent transport in the arterial wall under healthy and diseased conditions (Sections 2.1.3 and 2.1.4). A detailed

description of the computational geometry and the implementation of the model equations in a commercial finite element software is provided in Section 2.2. We then proceed to show the key results of the different simulations performed in Section 3. Finally, we present a discussion of the significance of the results in Section 4, highlighting the limitations and assumptions of the model.

2 Material and Methods

2.1 Governing equations

2.1.1 Modelling blood flow

In this work, blood is modelled as an incompressible Newtonian fluid governed by the steady Navier-Stokes equations and the continuity equation:

$$\rho_b(\boldsymbol{u}_l \cdot \nabla)\boldsymbol{u}_l = -\nabla p_l + \mu_b \nabla^2 \boldsymbol{u}_l, \tag{1}$$

where $\boldsymbol{u}_l$ and p_l are the velocity vector field and the pressure field of the blood flow in the lumen, respectively, and ρ_b and μ_b are the density and the dynamic viscosity of the blood, respectively. At the inlet of the lumen, $\Gamma_{l,inlet}$, a fully developed parabolic velocity profile is prescribed:

$$w_{l,inlet} = u_{max}\left(1 - \left(\frac{r}{r_l}\right)^2\right), \tag{2}$$

where w_l is the axial component of the blood velocity in the lumen; u_{max} is the centerline velocity for a typical value of the Reynolds number ($Re_l = \rho_b u_0 (2r_l)/\mu_b$) in the coronary artery of 400 corresponding to laminar flow [Formaggia et al., 2010]; r is the radial position, u_0 is the mean velocity and; r_l is the internal radius of the artery. A constant pressure of 100 mmHg is considered at the lumen outlet, $\Gamma_{l,outlet}$ [Ai and Vafai, 2006]. Moreover, the no-slip condition ($w_l = 0$) is prescribed at the endothelium, Γ_{et} [Vairo et al., 2010; Bozsak et al., 2014; Escuer et al., 2020]. We refer the reader to Fig. 1 for a schematic summarising the governing equations and the boundary conditions involved in the computational model.

2.1.2 Modelling porous media

The healthy arterial wall is modelled as a multilayered structure organised in three porous layers: subendothelial space (SES), media and adventitia. The plaque is also assumed to behave as a porous medium. Although it is well-known that atherosclerotic plaque composition is highly heterogeneous, in this work plaque is idealized as a fibrous cap with a core which may be lipid, necrotic or calcified, depending on the lesion considered. Due to the porous nature of the tissue, the flow field through the different regions of the arterial wall is calculated using the classical Darcy's law and the continuity equation:

$$\boldsymbol{u}_i = \frac{K_i}{\mu_p}\nabla p_i, \qquad \nabla \cdot \boldsymbol{u}_i = 0 \tag{3}$$

where the subscript $i = \{i_1, i_2\}$ denotes the healthy and unhealthy tissue regions, respectively; $i_1 = \{ses, m, a\}$ denotes the SES, the media and the adventitia, respectively; $i_2 = \{pfc, pc\}$ denotes the plaque's fibrous cap and the core of the plaque, respectively; $\boldsymbol{u}_i$ is the transmural velocity vector field; K_i is the Darcian permeability; μ_p is the dynamic viscosity of the plasma and; p_i is the pressure field. The Endothelium (ET), internal and external elastic laminae (IEL and EEL, respectively) are treated as semipermeable membranes and the fluid flux across them, $J_{v,j}$, is described by the Kedem-Katchalsky equations [Kedem and Katchalsky, 1958]. Neglecting the osmotic contribution as an approximation [Formaggia et al., 2010; Bozsak et al., 2014; Escuer et al., 2020], the Kedem-Katchalsky equations for fluid flux can be simplified as:

$$J_{v,j} = L_{p,j}\Delta p_j, \tag{4}$$

where the subscript $j = \{et, etp, iel, ielp, eel\}$ denotes the semipermeable membranes considered: the lumen-SES interface (et), the lumen-plaque interface (etp), the SES-media interface (iel), the plaque-media interface (ielp) and the media-adventitia interface (eel), respectively; $L_{p,j}$ is the membrane hydraulic conductivity and; Δp_j the pressure drop across each semipermeable membrane. The equations for the flux J_v, corresponding to each boundary, are shown in the Supplementary Material.

Due to the stent implantation, the endothelium is assumed to be denuded between stent struts and in zones distal and proximal to the stent over a distance that is one half of the interstrut spacing (ISS) measured from the respective stent strut centres [Bozsak et al., 2014] (Fig. 2). Outside of these regions the endothelium is assumed to be intact. In denuded regions, the volume flux across the endothelium simplifies to continuity of pressure, i.e. $p_l = p_{ses}$ under healthy conditions or $p_l = p_{pfc}$ in the presence of plaque in the outer wall of the artery. At the longitudinal wall boundaries, $\Gamma_{i_1,inlet}$ and $\Gamma_{i_1,outlet}$, in agreement with Bozsak et al. [2014]; Escuer et al. [2020], a zero-flow condition, $-\boldsymbol{n}_{i_1} \cdot \boldsymbol{u}_{i_1} = 0$, where $\boldsymbol{n}_{i_1}$ is the unit outward normal vector to the corresponding exterior boundary, is imposed. This choice of boundary condition is justified by

the fact that we are interested in computing drug concentrations only within the therapeutic domain while these boundaries are imposed sufficiently far upstream and downstream of the stented region. Moreover, it is assumed that the plasma cannot penetrate the surface of the polymer coating. At the perivascular side, Γ_a, a constant pressure of 30 mmHg [Ai and Vafai, 2006] is applied in order to set a physiologically realistic pressure drop of 70 mmHg between the lumen and the outer surface of the tissue [Meyer et al., 1996].

2.1.3 Modelling drug release from the stent coating

Drug release from a DES with non-erodible polymeric coating is modelled as a diffusion dominated process satisfying a simple diffusion equation [McGinty, 2014]:

$$\frac{\partial c_c}{\partial t} = \nabla \cdot (\boldsymbol{D}_c \nabla c_c), \tag{5}$$

where $c_c\,(r,z,t)$ is the volume-averaged concentration of free drug eluted from the stent coating and; $\boldsymbol{D}_c$ represents the diffusivity of the considered drug in the polymer. At t = 0, the drug is assumed to be completely contained within the polymer coating in dissolved phase (free drug) at uniform concentration, C_0. Continuity of drug concentration and mass flux is prescribed across the outer boundary of the polymeric stent coating, Γ_{ck}:

$$c_c = c_k, \tag{6}$$

$$(-\boldsymbol{D}_c \nabla c_c) \cdot \boldsymbol{n}_c = -(-\boldsymbol{D}_k \nabla c_k + \boldsymbol{u}_k c_k) \cdot \boldsymbol{n}_k, \tag{7}$$

where the subscript $k = \{l, pfc, m\}$ represents the lumen, the fibrous cap of the plaque and the media, respectively. Finally, we assume that the metallic strut is impermeable to the drug and therefore, a zero flux condition, $-\boldsymbol{n_c} \cdot (-\boldsymbol{D}_c \nabla c_c) = 0$, through the boundary surface between the metallic strut and the polymer coating, is imposed.

2.1.4 Modelling drug transport within the lumen and the arterial wall

Drug transport inside the arterial lumen is modelled as a time-dependent advection-diffusion process:

$$\frac{\partial c_l}{\partial t} + \boldsymbol{u}_l \cdot \nabla c_l = \nabla \cdot (\boldsymbol{D}_l \nabla c_l), \tag{8}$$

where $c_l\,(r,z,t)$ is the drug concentration within the fluid domain; $\boldsymbol{D}_l$ is the isotropic diffusivity of the drug in the blood and; $\boldsymbol{u}_l$ is the blood flow velocity calculated by Eq. (1). Likewise, drug transport processes in the SES and the adventitia may be written as:

$$\frac{\partial c_{ses}}{\partial t} + \frac{\gamma_{ses}}{\phi_{ses}} \boldsymbol{u}_{ses} \cdot \nabla c_{ses} = \nabla \cdot (\boldsymbol{D}_{ses} \nabla c_{ses}), \tag{9}$$

$$\frac{\partial c_a}{\partial t} + \frac{\gamma_a}{\phi_a} \boldsymbol{u}_a \cdot \nabla c_a = \nabla \cdot (\boldsymbol{D}_a \nabla c_a). \tag{10}$$

where the subscripts *ses* and a denote the SES and the adventitia, respectively, and; γ, ϕ, $\boldsymbol{u}$, $\boldsymbol{D}$ and $c\,(r,z,t)$ refer to the hindrance coefficients, porosities, transmural fluid velocities calculated by Eq. (3), diffusion coefficients and dissolved drug concentrations within the respective domains. In the media and plaque regions, drug dynamics are governed by the advection-diffusion-reaction equation:

$$\frac{\partial c_m}{\partial t} + \frac{\gamma_m}{\phi_m} \boldsymbol{u}_m \cdot \nabla c_m = \nabla \cdot (\boldsymbol{D}_m \nabla c_m) - \frac{\partial b_m^{ns}}{\partial t} - \frac{\partial b_m^{s}}{\partial t}, \tag{11}$$

$$\frac{\partial b_m^{ns}}{\partial t} = k_{on}^{ns} c_m (b_{max,m}^{ns} - b_m^{ns}) - k_{off}^{ns} b_m^{ns}, \tag{12}$$

$$\frac{\partial b_m^{s}}{\partial t} = k_{on}^{s} c_m (b_{max,m}^{s} - b_m^{s}) - k_{off}^{s} b_m^{s}. \tag{13}$$

$$\frac{\partial c_{i_2}}{\partial t} + \frac{\gamma_{i_2}}{\phi_{i_2}} \boldsymbol{u}_{i_2} \cdot \nabla c_{i_2} = \nabla \cdot (\boldsymbol{D}_{i_2} \nabla c_{i_2}) - \frac{\partial b_{i_2}}{\partial t}, \tag{14}$$

$$\frac{\partial b_{i_2}}{\partial t} = k_{on}^{ns} c_{i_2} (b_{max,i_2} - b_{i_2}) - k_{off}^{ns} b_{i_2}, \tag{15}$$

where the subscripts m and i_2 denote parameters and variables with respect to the media and plaque layers, respectively, and superscripts s and ns denotes specific and non-specific binding, respectively. Eqs. (12) and (13) describe a nonlinear saturable reversible binding model to adequately account for the drug binding process in the media [Tzafriri et al., 2012; McGinty and Pontrelli, 2016; McKittrick et al., 2019]. This reaction model is able to define three different states of the drug in the media layer: drug dissolved in the plasma, $c_m\,(r,z,t)$, drug bound to specific binding sites (target receptors), $b_m^s\,(r,z,t)$, and drug bound to non-specific binding sites (general ECM sites), $b_m^{ns}\,(r,z,t)$. Due to the lack of binding data available in the literature for the plaque, we have considered a single phase nonlinear saturable reversible binding model in these regions, Eq. (15), and only two different states of the drug can be defined: drug dissolved in the plasma, $c_{i2}\,(r,z,t)$ and drug bound to components of plaque, $b_{i2}\,(r,z,t)$. The binding rate constants (forward reaction rates) are given by k_{on}^s and k_{on}^{ns} whereas the unbinding rate constants (reverse reaction rates) are given by k_{off}^s and k_{off}^{ns}. In the plaque regions, these are assumed to take the same values as the non-specific rates in the media. The rate constants are related through the equilibrium dissociation constants, K_d^s and K_d^{ns}, which are defined as

$K_d^s = k_{off}^s/k_{on}^s$ and $K_d^{ns} = k_{off}^{ns}/k_{on}^{ns}$. The parameters $b_{max,m}^s$, $b_{max,m}^{ns}$ and b_{max,i_2} are the maximum density of binding sites in the media (specific, non-specific) and in the plaque region, respectively. Discontinuity of solute flux across the semipermeable membranes, $J_{s,j}$, is governed by the Kedem-Katchalsky equations [Kedem and Katchalsky, 1958]:

$$J_{s,j} = P_j \Delta c_j + s_j \bar{c}_j J_{v,j} \tag{16}$$

where P_j is the permeability of each semipermeable membrane; Δc_j is the solute concentration difference; s_j is the sieving coefficient and; $\bar{c}_j$ is the weighted average concentration on either side of the corresponding membrane [Levitt, 1975]. The equations for the flux J_s corresponding to each boundary are shown in the Supplementary Material. Continuity of flux and concentration is assumed on the fibrous cap-plaque core interface, Γ_p. Note that when a calcified lesion is considered in the simulations, the plaque core is assumed to be impermeable to all species present in adjacent regions. This assumption is in agreement with Ferreira et al. [2017] and echoes Tzafriri et al. [2017] where it was found that, at least for paclitaxel, diffusion in dense and calcified plaque is significantly hindered, potentially up to 300-fold. In the lumen, a zero drug concentration boundary condition is applied at the inlet, $c_l = 0$, and an outflow condition, $-\boldsymbol{n}_l \cdot (-\boldsymbol{D}_l \nabla c_l) = 0$, is applied at the outlet. Following Vairo et al. [2010], the upstream and downstream boundaries of the tissue are subjected to a zero-flux condition: $-\boldsymbol{n}_{i_1} \cdot (-\boldsymbol{D}_{i_1} \nabla c_{i_1} + \boldsymbol{u}_{i_1} c_{i_1}) = 0$. Finally, a perfect sink condition for the free drug is applied at the perivascular side, $c_a = 0$ [Bozsak et al., 2014; Escuer et al., 2020].

[Fig. 1 about here.]

2.2 Computational model

2.2.1 Geometry of the model

Several 2D computational models corresponding to idealised longitudinal sections of segments of coronary arteries have been considered in this work as a first step for performing a comprehensive analysis of the influence of arterial curvature and plaque composition on drug transport within the arterial wall. To study the effect of the arterial curvature, six different geometries of a healthy coronary artery containing a DES have been analysed: one corresponding to a straight segment and the remaining five corresponding to curved segments of varying curvature. The curvature of a vessel can be defined by the curvature ratio, κ, which is calculated as [Santamarina et al., 1998]:

$$\kappa = \frac{r_l}{R} \tag{17}$$

where r_l is the lumen radius and R is the curvature radius of the vessel measured in the centreline of the artery. The average curvature ratio of a coronary artery is approximately 0.1 [Jayarama, 2006], but varies greatly depending on the particular location, lying in the range of 0.02-0.5 [Santamarina et al., 1998]. In Fig. 2a, the geometry for the case with average curvature ratio is shown. Moreover, to investigate the impact of plaque composition, a stenosed curved segment (with $\kappa = 0.1$) of a coronary artery with an eccentric atherosclerotic plaque located between the DES and the media layer within the inner wall of the vessel have been taken into account (Fig. 2b). The length of the arterial segments remains constant in all cases studied. A schematic showing the geometry of all investigated cases is shown in Fig. 3. The healthy arterial wall is modelled as a three-layered structure with the subendothelial space (SES), the media and the adventitia defined as distinct domains (Ω_{ses}, Ω_m and Ω_a, respectively), while the endothelium, Γ_{et}, the internal elastic lamina, Γ_{iel}, and the external elastic lamina, Γ_{eel}, are modelled as semipermeable membranes of negligible thickness between these layers. The plaque is composed of two different domains: fibrous cap, Ω_{pfc}, and core, Ω_{pc}. The length of the plaque (approximately 6 mm) and the percentage of diameter stenosis (20 %) correspond to values within the range found in the literature [Hossain et al., 2012; Rozie et al., 2009; Kosa et al., 1999; Kern et al., 1999]. The device is represented by ten circular struts half-embedded the tissue in all simulations. The ISS in each case will change with the curvature of the segment, with the centre of each strut being projected radially. This means that the ISS will be different for the inner and outer wall and will be also affected by the presence of the plaque. The lumen geometry was extended at both ends (not shown in Figs. 2 and 3) by a length equivalent to five diameters, in order to obtain a fully-developed flow near the DES and to avoid effects associated with the constraints applied at the inlet and the outlet boundaries, thereby reducing their influence on the results [Chiastra et al., 2014]. Parameters related to the computational geometry such as the internal artery radius, r_l; layer thicknesses, δ_i; metallic strut diameter, d_{strut}, and; polymer thickness, δ_p, are taken from the existing literature and are listed in Table 1.

[Table 1 about here.]

[Fig. 2 about here.]

[Fig. 3 about here.]

2.2.2 Numerical methods

The commercial finite element (FE) package COMSOL Multiphysics 5.3a (COMSOL AB, Burlington, MA, USA) was used to build the mesh and to numerically solve the governing equations described in Section 2 for the different cases considered. The computational analysis was conducted in two steps: (1) a stationary analysis of blood flow dynamics and plasma filtration and; (2) a time-dependent drug transport analysis coupled with the solutions of luminal and transmural flow computed in the previous step. A sensitivity analysis was carried out in order to evaluate the influence of the mesh and time-step size on the solution. Mesh density and time-step independence was assumed when there was less than 1% difference in the time varying profiles of normalised mean concentration (NMC) in the media layer after several mesh and time-step refinements. The computational domains were discretized in space using triangular elements, resulting in an overall mesh with approximately 885,000 elements in case of healthy conditions (geometries without plaque) and more than 950,000 elements under pathological conditions. The discretization employs Lagrange P3-P2 elements for the blood dynamics problem and quadratic Lagrange elements for the porous media and drug dynamics problems, respectively. Details of the mesh used in the different regions of the computational model are illustrated in Fig. 2c. A direct linear solver (MUMPS) was used to solve the stationary step with a tolerance for the relative error of the solution of 10^{-3}. The backward differentiation formula (BDF) method was used for the time discretization of the transient step, with variable order of accuracy between 1 and 5 and variable time-step size. The relative and absolute tolerance was set to 10^{-3} and 10^{-4}, respectively. The resulting system of time-dependent partial differential equations (PDEs) is solved using a direct linear solver (PARDISO) with a nested dissection preordering algorithm. Using 14 cores of an Intel® Core™ i9-10940X CPU @ 3.30 GHz processor, the computation time for each of the 9 cases varies between 15 and 20 hours.

2.2.3 Model parameters

To date, the drugs most widely used in drug-eluting stents are sirolimus and its analogues such as everolimus or zotarolimus. Sirolimus and derivatives are antiproliferative agents that target the FK506 binding protein 12 (FKBP12). This complex subsequently binds to the mammalian target of rapamycin (mTOR) and thereby interrupts the cell cycle from the G1 to the S phase [Martin and Boyle, 2011]. In the numerical simulations, sirolimus has been considered. Wherever possible, transport and binding parameters for sirolimus and physiological parameters related with the blood flow and porous media have been obtained from existing published experimental data. The values of these model parameters have been included in Table 2.

[Table 2 about here.]

2.2.4 Summary of investigated cases

We start by simulating the straight artery model (corresponding to $\kappa = 0$) and then we simulate five different curvature ratios ranging from $\kappa = 0.025$ to $\kappa = 0.4$. Finally, in order to analyse the impact of atherosclerotic plaques on curved vessels on drug transport, three different types of plaque, varying the composition of the core (fibrotic, lipid or calcified core), are compared for the case of average arterial curvature ($\kappa = 0.1$). The list of cases simulated are summarised in Table 3. In all cases we assume an initial drug concentration in the stent coating, C_0, of 100 mol m^{-3} [Bozsak et al., 2014].

[Table 3 about here.]

2.3 Analysis of the results

In order to effect comparisons between the different cases (Table 3), we will show the time-varying profiles of normalised mean concentration (NMC) and spatially-varying profiles of normalised local concentration (NLC). These results are typically shown over the first 12 - 24 hours since this is where the largest differences have been observed for the parameter values simulated. However, we also show 2D results over 7 days. In the Supplementary Material we extend the results to 30 days. Furthermore, we also calculate the percentage of binding sites that are saturated as a function of time, a quantity strongly linked with efficacy, and display the results over 30 days. The results presented in this work are focussed on the drug distribution in the arterial wall since the drug concentration in the blood is typically 3-4 orders of magnitude lower than in the tissue (Fig. S23 of the Supplementary Material).

2.3.1 Normalised mean concentration (NMC)

The total NMC in each region of the curved artery at any time point is evaluated by averaging the total concentration over its respective spatial domain as follows:

$$Total\ NMC_i\ (t) = \frac{1}{A_i \cdot C_0} \int_{A_i} (c_i + b_i^s + b_i^{ns})\, dA, \quad (18)$$

where A_i is the area of the region i, that falls within the therapeutic domain considered. The free and bound NMC (both specific and non-specific) of drug in each domain of the arterial wall at any time point are evaluated by averaging the free and bound (specific, S, and non-specific, NS) concentration over its respective spatial domain as follows:

$$Free\ NMC_i\ (t) = \frac{1}{A_i \cdot C_0} \int_{A_i} c_i\ dA, \tag{19}$$

$$S\ Bound\ NMC_i\ (t) = \frac{1}{A_i \cdot C_0} \int_{A_i} b_i^s\ dA. \tag{20}$$

$$NS\ Bound\ NMC_i\ (t) = \frac{1}{A_i \cdot C_0} \int_{A_i} b_i^{ns}\ dA. \tag{21}$$

2.3.2 Normalised local concentration (NLC)

The total, free and bound NLC in each region of the curved artery are calculated as follows:

$$Total\ NLC_i = (c_i + b_i^s + b_i^{ns})/C_0, \tag{22}$$

$$Free\ NLC_i = c_i/C_0, \tag{23}$$

$$S\ Bound\ NLC_i = b_i^s/C_0, \tag{24}$$

$$NS\ Bound\ NLC_i = b_i^{ns}/C_0. \tag{25}$$

2.3.3 Binding sites % saturation (% BSS)

The binding site % saturation as a function of time is calculated as [McKittrick et al., 2019]:

$$\%\ SBSS\ (t) = \frac{100}{A_i \cdot b_{max,i}^s} \int_{A_i} b_i^s\ dA_i. \tag{26}$$

$$\%\ NSBSS\ (t) = \frac{100}{A_i \cdot b_{max,i}^{ns}} \int_{A_i} b_i^{ns}\ dA_i. \tag{27}$$

Note that the interaction between the drug and the tissue is only considered in the media and in the plaque regions, therefore the bound NMC, the bound NLC and the % BSS in the SES and in the adventitia are zero by definition. Moreover, binding is not modelled as separated phases in the plaque, therefore in these regions the bound NMC and the bound NLC refer to total bound drug and % BSS refers to general binding sites.

3 Results

3.1 Effect of arterial curvature

The temporal variation of NMC of sirolimus within each layer of the arterial wall, obtained for the simulations corresponding to the straight artery ($\kappa = 0$) and five different degrees of curvature ($\kappa = 0.025 - 0.4$) under healthy conditions (without plaque) is displayed in Fig. 4. Firstly, our results show that the inner wall is more sensitive to changes in κ than the outer wall. Specifically, there is a greater difference between NMC profiles when κ is varied in the inner wall compared with the outer wall. Interestingly, in the inner wall the total NMC in each layer increases with increasing κ, yet in the outer wall the reverse trend is observed.

[Fig. 4 about here.]

Since binding is only considered in the media, in Fig. 5 we separate-out free NMC from bound NMC (specific and non-specific) in this layer. From these plots it is evident that, for both the inner and outer wall, differences in total NMC as κ is varied are primarily as a result of differences in free NMC, i.e. there is little variation in bound drug NMC as κ is varied. However, there is a clear trend for higher binding site saturation levels in the inner wall with increasing κ, with the opposite trend observed in the outer wall (Fig. 6).

[Fig. 5 about here.]

[Fig. 6 about here.]

In Fig. 7 we display spatially-varying profiles of total NLC of sirolimus in the arterial wall at four different times after stent implantation in a radial section between the middle struts (struts 5 and 6 in each wall). Similar trends are observed as with NMC, i.e. an increase in NLC concentrations with increasing κ in the inner wall and the reverse trend in the outer wall. At early times (10 mins), the differences are most notable in the media layer, while at intermediate times (1-4 hours), where the drug has reached the adventitia, these trends are observed across the entire arterial wall. Interestingly, at later times (24 hours) the NLC concentrations are virtually indistinguishable. In Fig. 8 we also show 2D results over 7 days for curvature ratios of $\kappa = 0.1$ (average curvature) and $\kappa = 0.4$ (maximum curvature). The corresponding plots for the spatially-varying profiles of free and bound (specific and non-specific) NLC and binding site % saturation levels, supporting the idea that differences between the inner and outer wall are driven by differences in free drug concentrations, may be found in the Supplementary Material (Figs. S3-S7).

[Fig. 7 about here.]

In Fig. 8 we plot the spatial variation of total NLC across the inner wall tissue domain and compare $\kappa = 0.1$ with $\kappa = 0.4$ for the first 7 days. This plot shows clear differences in drug deposition, with the higher curvature leading to higher NLC of drug, with the effect most prominent at early times.

[Fig. 8 about here.]

3.2 Effect of plaque composition

The time-varying profiles of total NMC of drug for four regions of the inner wall (fibrous cap, plaque core, media and adventitia) of a stented curved segment of an artery ($\kappa = 0.1$) under pathological conditions are illustrated in Fig. 9. The results are shown for three different plaque core compositions: fibrotic, lipid and calcified. Fig. 9a displays the total NMC in the fibrous cap, assuming different compositions of plaque core. We observe that the NMC profile is similar regardless of whether the plaque core is fibrotic or lipid, but when the core is considered calcified the peak NMC is approximately 13% greater and the NMC profile tracks slightly below the fibrotic and lipid core cases beyond day 5. This is likely due to the impenetrable nature of the calcification. Fig. 9b clearly shows that the plaque composition impacts on the total NMC of drug within the plaque, with a lipid core giving rise to higher NMC levels than a fibrotic core. When we probe the split between free and bound drug (Figs. S14b - S15b) we find that the higher NMC in the lipid core is primarily as a result of the higher levels of bound drug, following the higher density of drug binding sites. Since the model assumes that calcified plaque is impenetrable to drug, the total NMC is zero by definition. Fig. 9c and 9d show not only that the presence of plaque significantly influences the time-varying total NMC of drug within the media and adventitia, respectively, but also that the composition of the plaque core leads to modest variation in the total NMC of drug within these layers. The presence of the plaque leads to a delay and reduction in magnitude of the peak NMC of drug in the media; however, the plaque appears to act as source for drug, ensuring that NMC drug levels in the media are maintained at higher levels for longer. Whilst there is a slight delay in peak bound drug NMC in the media (Figs. S15c - S15d), receptors and ECM binding sites are saturated at higher levels for longer in the case of the presence of plaque (Fig. S16). The corresponding spatially-varying profiles of total NLC of sirolimus within the plaque and arterial wall at four different times after stent implantation are shown in Fig. 10. The rest of the figures for the temporal profiles of NMC and binding site % saturation (Figs. S14 - S16) and for the spatially-varying profiles of NLC (Figs. S17 - S21) may be found in the Supplementary Material.

[Fig. 9 about here.]

[Fig. 10 about here.]

4 Discussion

This study has yielded a number of interesting points that we wish to emphasize. Our results clearly demonstrate that curvature leads to the asymmetric distribution of drug in the arterial wall, with the level of asymmetry highly dependent on the level of curvature. Specifically, with increasing curvature, more of the drug 'partitions' into the inner wall. We have established (Supplementary Material) that the total mass of drug delivered to the wall is consistent, regardless of level of curvature, and that the level of curvature does not influence the drug release rate. To probe this further, we calculated the Dean number ($De_l = Re_l\sqrt{\kappa}$) for the flow in the curved vessel and Peclet number for transport in the wall under healthy conditions. There is a nonlinear increase in Dean number with curvature and consequent asymmetry in the fluid flow pattern in the lumen (Figs. S24 and S25 of the Supplementary Material, respectively). In Fig. S26 of the Supplementary Material we plot the magnitude of the radial component of the plasma filtration velocity and the radial Peclet number ($Pe_{r,i1} = u_{r,i1}\delta_{i1}/D_{r,i1}$) across the inner and outer walls of the artery, respectively, for the different cases of curvature. These plots suggest that curvature has the effect of increasing the radial Peclet number in the inner wall more than in the outer wall, as a result of increased plasma filtration. This asymmetric distribution, as a result of fluid forces, is likely to be exacerbated in more realistic patient-specific geometries. The implication of this finding for stent manufacturers is that care should be taken when considering the drug loading on the stent, since this asymmetric drug distribution could, in theory at least, result in insufficient drug concentrations reaching the outer wall, while the concentrations reaching the inner wall could be too high. The consequence for the patient could well be asymmetric neointimal growth as part of the healing process. While it is now possible to reconstruct patient-specific 3D lumen geometries [Chiastra et al., 2018], further work is required to develop robust methods for accurate reconstruction of the wall that discriminates between different components of tissue and plaque. Even when such methodologies are available, a severe limitation is accurate characterization of tissue and plaque properties.

Plaque core composition greatly influences drug concentrations within the plaque core itself, owing to the differing density of binding sites. Our results suggest that lipidic plaques give rise to higher drug concentrations than fibrotic plaques, while calcified plaques are impenetrable to drug as per our model assumptions. The impenetrability of calcified plaque has potentially important implications and if large enough in extent, may act as a significant barrier to drug reaching the arterial tissue where proliferating and migrating cells reside. Indeed, Tzafriri et al. [2017] demonstrated that calcified plaque limits intravascular drug delivery and found that controlled orbital atherectomy can lead to improved drug delivery. Our results suggest that the presence of plaque, regardless of the composition of the core, can slightly delay receptor saturation in the media, a quantity that has widely been associated with efficacy (e.g. Tzafriri et al. [2012] and McKittrick et al. [2019]). Perhaps more importantly, our results indicate that plaque can act as a source of drug ensuring that decline in receptor saturation is significantly reduced compared with the healthy case. This is in agreement with the somewhat simpler one-dimensional model devised by McGinty et al. [2010] who noted that the plaque may act as a reservoir for drug. The implication is that in diseased states, binding sites may well be saturated for longer, i.e. patients receive an effective drug dose for longer. However, these findings differ from those reported in the work of Tzafriri et al. [2010], where it was found, somewhat counter-intuitively, that drug content in human aortae inversely correlated with lipid content. One potential explanation provided, specifically for paclitaxel, was the displacement of tubulin-expressing cells by lipid pools, potentially important given paclitaxel's ability to bind specifically to tubulin. Since our findings reveal that drug distribution and retention is dependent on plaque composition, stent manufacturers are advised to consider that a 'one-size-fits-all' stent drug dose may not be adequate for all patients, and could, at least in part, be contributing to differences in outcome from patient-to-patient that are observed clinically.

4.1 Limitations of this work

We should emphasize that the results in the present paper are heavily dependent on the model parameter values and binding model employed for the different types of plaque. This is primarily because there is a lack of data available in the literature for the different components of plaque to fully parametrize such a model. We have taken the majority of our plaque parameter values from the literature, but necessarily have had to estimate some of them (Table 2). Given the paucity of data on drug transport and binding properties of atherosclerotic plaque, despite the obvious importance and relevance to the condition being treated by stents, there is an urgent need for further research in this area so that models such as the one presented here may be furnished with the most realistic and reliable parameter values. This is the key limitation of the present work, although we now comprehensively discuss the remaining limitations.

We have employed a simplified 2D coronary artery model with curvature in this study. Our plaque geometry is also a simplification. The geometry we have chosen is based on Lee and Libby [1997] and incorporates the general features of human atherosclerotic plaque: a core that can be either lipid, fibrous or calcified, surrounded by fibrous tissue. What tends to be observed clinically are plaques consisting of multiple material components, in often complex geometrical configurations, with vulnerable plaques in particular typically displaying a thin fibrous cap separating a lipid rich core from the lumen. The plaque composition, structure and geometry in reality is patient-specific, with each of these likely to affect drug distribution.

While 3D patient-specific models are now common when considering haemodynamics in stented arteries, these models often neglect, or do not adequately consider the state-of-the art in terms of modelling drug release and retention. There are many aspects related to drug release and subsequent redistribution in tissue that we do not fully understand, which is why the majority of models focussing on the drug kinetics are still considering lower-dimensional models. In this work we focussed on two of these aspects, curvature and plaque composition, with our results providing evidence to support the investigation of a 3D patient-specific model in the future.

In this work, the complex geometry of the stent is simplified to ten equally spaced circular struts. We have verified that using square struts with the same coating area and drug loading gives rise to results that are almost indistinguishable. We appreciate that there are a variety of stents on the market of varying strut size, coating thickness and drug loading. Comparing these aspects was not the focus of this study, although we note that varying each of these aspects will have an impact on the results.

In terms of modelling drug release from the stent coating, a simple diffusion model is considered in this work in line with a large number of mathematical and computational models in the existing literature. The diffusion coefficient we have selected is at the upper end of the range considered in the literature, and im-

plies fast release kinetics. However, depending on the particular stent, drug and coating under consideration, a more complex nonlinear model that accounts for the combined effects of diffusion, dissolution and solubility in the polymer coating may be required in order to describe drug release from the device [McGinty and Pontrelli, 2015].

4.2 Conclusions

In this paper we have provided a comprehensive study of the influence of the vessel curvature and plaque composition on drug transport within the arterial wall, described as a multi-layer anisotropic structure, under healthy and pathological conditions. We have performed 2D idealized simulations to quantify the impact of such geometrical and compositional variation on spatio-temporal uptake of drug in tissue. Our findings demonstrate that arterial curvature and plaque composition have important influences on the spatio-temporal distribution of drug, with potential implications in terms of effectiveness of the treatment. Since the majority of computational models tend to neglect these features, these models are likely to be under- or over-estimating drug uptake and redistribution in arterial tissue.

Acknowledgements This work was funded by the Spanish Ministry of Economy, Industry and Competitiveness through research project number DPI2016-76630-C2-1-R and grant number BES-2014-069737; the Department of Industry and Innovation (Government of Aragon) through research group grant number T24-17R (Fondo Social Europeo) and research project number LMP121-18 and; the Carlos III Health Institute (ISCIII) through the CIBER initiative. Dr. McGinty acknowledges funding provided by EPSRC (Grant number EP/S030875/1).

Conflict of interest The authors declare that they have no conflict of interest.

References

Ai L, Vafai K (2006) A coupling model for macromolecule transport in a stenosed arterial wall. International Journal of Heat and Mass Transfer 49(9-10):1568–1591

Alfonso F, Byrne RA, Rivero F, Kastrati A (2014) Current treatment of in-stent restenosis. Journal of the American College of Cardiology 63(24):2659–2673

Bierer BE, Mattila PS, Standaert RF, Herzenberg LA, Burakoff SJ, Crabtree G, Schreiber SL (1990) Two distinct signal transmission pathways in t lymphocytes are inhibited by complexes formed between an immunophilin and either fk506 or rapamycin. Proceedings of the National Academy of Sciences 87(23):9231–9235

Bozsak F, Chomaz JM, Barakat AI (2014) Modeling the transport of drugs eluted from stents: physical phenomena driving drug distribution in the arterial wall. Biomechanics and Modeling in Mechanobiology 13(2):327–347

Byrne RA, Joner M, Kastrati A (2015) Stent thrombosis and restenosis: what have we learned and where are we going? the andreas grüntzig lecture esc 2014. European Heart Journal 36(47):3320–3331

Caputo M, Chiastra C, Cianciolo C, Cutrì E, Dubini G, Gunn J, Keller B, Migliavacca F, Zunino P (2013) Simulation of oxygen transfer in stented arteries and correlation with in-stent restenosis. International journal for numerical methods in biomedical engineering 29(12):1373–1387

Chiastra C, Migliavacca F, Martínez MÁ, Malvè M (2014) On the necessity of modelling fluidstructure interaction for stented coronary arteries. Journal of the Mechanical Behavior of Biomedical Materials 34:217–230

Chiastra C, Migliori S, Burzotta F, Dubini G, Migliavacca F (2018) Patient-specific modeling of stented coronary arteries reconstructed from optical coherence tomography: Towards a widespread clinical use of fluid dynamics analyses. Journal of cardiovascular translational research 11(2):156–172

Creel CJ, Lovich MA, Edelman ER (2000) Arterial paclitaxel distribution and deposition. Circulation Research 86(8):879–884

Cutrì E, Zunino P, Morlacchi S, Chiastra C, Migliavacca F (2013) Drug delivery patterns for different stenting techniques in coronary bifurcations: a comparative computational study. Biomechanics and Modeling in Mechanobiology 12(4):657–669

Escuer J, Cebollero M, Peña E, McGinty S, Martínez MA (2020) How does stent expansion alter drug transport properties of the arterial wall? Journal of the Mechanical Behavior of Biomedical Materials p 103610

Ferreira JA, Gonçalves L, Naghipoor J, de Oliveira P, Rabczuk T (2017) The influence of atherosclerotic plaques on the pharmacokinetics of a drug eluted from bioabsorbable stents. Mathematical Biosciences 283:71–83

Ferreira JA, Gonçalves L, Naghipoor J, de Oliveira P, Rabczuk T (2018) The effect of plaque eccentricity on blood hemodynamics and drug release in a stented artery. Medical Engineering & Physics 60:47–60

Formaggia L, Quarteroni A, Veneziani A (2010) Cardiovascular Mathematics: Modeling and simulation

of the circulatory system, vol 1. Springer Science & Business Media

Frangos SG, Gahtan V, Sumpio B (1999) Localization of atherosclerosis: role of hemodynamics. Archives of Surgery 134(10):1142–1149

Hossain SS, Hossainy SF, Bazilevs Y, Calo VM, Hughes TJ (2012) Mathematical modeling of coupled drug and drug-encapsulated nanoparticle transport in patient-specific coronary artery walls. Computational Mechanics 49(2):213–242

Jayarama G (2006) Flow in tubes with complicated geometries with special application to blood flow in large arteries. In: Biomathematics: Modelling and Simulation, World Scientific, pp 279–304

Karner G, Perktold K (2000) Effect of endothelial injury and increased blood pressure on albumin accumulation in the arterial wall: a numerical study. Journal of biomechanics 33(6):709–715

Karner G, Perktold K, Zehentner HP (2001) Computational modeling of macromolecule transport in the arterial wall. Computer Methods in Biomechanics and Biomedical Engineering 4(6):491–504

Kedem O, Katchalsky A (1958) Thermodynamic analysis of the permeability of biological membranes to non-electrolytes. Biochimica et Biophysica Acta 27:229–246

Kern MJ, Puri S, Bach RG, Donohue TJ, Dupouy P, Caracciolo EA, Craig WR, Aguirre F, Aptecar E, Wolford TL, et al. (1999) Abnormal coronary flow velocity reserve after coronary artery stenting in patients: role of relative coronary reserve to assess potential mechanisms. Circulation 100(25):2491–2498

Kosa I, Blasini R, Schneider-Eicke J, Dickfeld T, Neumann FJ, Ziegler S, Matsunari I, Neverve J, Schömig A, Schwaiger M (1999) Early recovery of coronary flow reserve after stent implantation as assessed by positron emission tomography. Journal of the American College of Cardiology 34(4):1036–1041

LaDisa JF, Guler I, Olson LE, Hettrick DA, Kersten JR, Warltier DC, Pagel PS (2003) Three-dimensional computational fluid dynamics modeling of alterations in coronary wall shear stress produced by stent implantation. Annals of biomedical engineering 31(8):972–980

Lee RT, Libby P (1997) The unstable atheroma. Arteriosclerosis, thrombosis, and vascular biology 17(10):1859–1867

Levin AD, Vukmirovic N, Hwang CW, Edelman ER (2004) Specific binding to intracellular proteins determines arterial transport properties for rapamycin and paclitaxel. Proceedings of the National Academy of Sciences of the United States of America 101(25):9463–9467

Levitt DG (1975) General continuum analysis of transport through pores. i. proof of onsager's reciprocity postulate for uniform pore. Biophysical Journal 15(6):533–551

Lovich MA, Edelman ER (1996) Computational simulations of local vascular heparin deposition and distribution. American Journal of Physiology-Heart and Circulatory Physiology 271(5):H2014–H2024

Mandal AP, Mandal PK (2018) Distribution and retention of drug through an idealised atherosclerotic plaque eluted from a half-embedded stent. International Journal of Dynamics and Control 6(3):1183–1193

Martin DM, Boyle FJ (2011) Drug-eluting stents for coronary artery disease: a review. Medical Engineering & Physics 33(2):148–163

McGinty S (2014) A decade of modelling drug release from arterial stents. Mathematical Biosciences 257:80–90

McGinty S, Pontrelli G (2015) A general model of coupled drug release and tissue absorption for drug delivery devices. Journal of Controlled Release 217:327–336

McGinty S, Pontrelli G (2016) On the role of specific drug binding in modelling arterial eluting stents. Journal of Mathematical Chemistry 54(4):967–976

McGinty S, McKee S, Wadsworth RM, McCormick C (2010) Modelling drug-eluting stents. Mathematical Medicine and Biology: a journal of the IMA 28(1):1–29

McKittrick C, Kennedy S, Oldroyd K, McGinty S, McCormick C (2016) Modelling the impact of atherosclerosis on drug release and distribution from coronary stents. Annals of Biomedical Engineering 44(2):477–487

McKittrick CM, McKee S, Kennedy S, Oldroyd K, Wheel M, Pontrelli G, Dixon S, McGinty S, McCormick C (2019) Combining mathematical modelling with in vitro experiments to predict in vivo drug-eluting stent performance. Journal of Controlled Release 303:151–161

Meyer G, Merval R, Tedgui A (1996) Effects of pressure-induced stretch and convection on low-density lipoprotein and albumin uptake in the rabbit aortic wall. Circulation Research 79(3):532–540

Mongrain R, Leask R, Brunette J, Faik I, Bulman-Feleming N, Nguyen T (2005) Numerical modeling of coronary drug eluting stents. Studies in Health Technology and Informatics 113:443–458

Naghipoor J, Rabczuk T (2017) A mechanistic model for drug release from plga-based drug eluting stent: A computational study. Computers in Biology and Medicine 90:15–22

Roth GA, Abate D, Abate KH, Abay SM, Abbafati C, Abbasi N, Abbastabar H, Abd-Allah F, Abdela J, Abdelalim A, et al. (2018) Global, regional, and national age-sex-specific mortality for 282 causes of death in 195 countries and territories, 1980–2017: a systematic analysis for the global burden of disease study 2017. The Lancet 392(10159):1736–1788

Rozie S, De Weert T, De Monyé C, Homburg P, Tanghe H, Dippel D, Van der Lugt A (2009) Atherosclerotic plaque volume and composition in symptomatic carotid arteries assessed with multidetector ct angiography; relationship with severity of stenosis and cardiovascular risk factors. European Radiology 19(9):2294–2301

Santamarina A, Weydahl E, Siegel JM, Moore JE (1998) Computational analysis of flow in a curved tube model of the coronary arteries: effects of time-varying curvature. Annals of Biomedical Engineering 26(6):944–954

Tarbell JM (2003) Mass transport in arteries and the localization of atherosclerosis. Annual Review of Biomedical Engineering 5(1):79–118

Tzafriri AR, Levin AD, Edelman ER (2009) Diffusion-limited binding explains binary dose response for local arterial and tumour drug delivery. Cell Proliferation 42(3):348–363

Tzafriri AR, Vukmirovic N, Kolachalama VB, Astafieva I, Edelman ER (2010) Lesion complexity determines arterial drug distribution after local drug delivery. Journal of Controlled Release 142(3):332–338

Tzafriri AR, Groothuis A, Price GS, Edelman ER (2012) Stent elution rate determines drug deposition and receptor-mediated effects. Journal of Controlled Release 161(3):918–926

Tzafriri AR, Garcia-Polite F, Zani B, Stanley J, Muraj B, Knutson J, Kohler R, Markham P, Nikanorov A, Edelman ER (2017) Calcified plaque modification alters local drug delivery in the treatment of peripheral atherosclerosis. Journal of Controlled Release 264:203–210

Vairo G, Cioffi M, Cottone R, Dubini G, Migliavacca F (2010) Drug release from coronary eluting stents: a multidomain approach. Journal of Biomechanics 43(8):1580–1589

Wang S, Vafai K (2015) Analysis of low density lipoprotein (ldl) transport within a curved artery. Annals of Biomedical Engineering 43(7):1571–1584

Wear MA, Walkinshaw MD (2007) Determination of the rate constants for the fk506 binding protein/rapamycin interaction using surface plasmon resonance: An alternative sensor surface for ni2+–nitrilotriacetic acid immobilization of his-tagged proteins. Analytical Biochemistry 371(2):250–252

Zunino P (2004) Multidimensional pharmacokinetic models applied to the design of drug-eluting stents. Cardiovascular Engineering: An International Journal 4(2):181–191

Table 1 List of the geometrical parameters related to the computational models.

Parameter	Description	Value	Reference
r_l	Lumen radius	1.5 mm	Mongrain et al. [2005]
δ_{ses}	Intima thickness	0.01 mm	Karner et al. [2001]
δ_m	Media thickness	0.5 mm	Vairo et al. [2010]
δ_a	Adventitia thickness	0.4 mm	Creel et al. [2000]
d_{strut}	Metallic strut diameter	0.15 mm	Mongrain et al. [2005]
δ_p	Polymeric coating thickness	0.05 mm	Mongrain et al. [2005]

Table 2 List of model parameters.

Parameter	Description	Value	Reference
Δp	Pressure difference across the arterial wall	70 mmHg	Meyer et al. [1996]
Re_l	Lumenal Reynolds number	400	Formaggia et al. [2010]
ρ_b	Blood density	1060 kg m^{-3}	LaDisa et al. [2003]
ρ_p	Plasma density	1060 kg m^{-3}	Bozsak et al. [2014]
μ_b	Blood dynamic viscosity	$3.5 \cdot 10^{-3}$ Pa s	Karner and Perktold [2000]
μ_p	Plasma dynamic viscosity	$7.2 \cdot 10^{-4}$ Pa s	Zunino [2004]
ϕ_{ses}	Porosity of the intima	0.983	Ai and Vafai [2006]
ϕ_m	Porosity of the media	0.258	Ai and Vafai [2006]
ϕ_a	Porosity of the adventitia	0.85	Lovich and Edelman [1996]
ϕ_{pfc}	Porosity of the fibrous cap	0.75	Ferreira et al. [2017]
ϕ_{pc}	Porosity of the plaque core (fibrotic)	0.75	Ferreira et al. [2017]
ϕ_{pc}	Porosity of the plaque core (lipid)	0.5	Naghipoor and Rabczuk [2017]
ϕ_{pc}	Porosity of the plaque core (calcified)	0	Ferreira et al. [2017]
γ_{ses}	Hindrance coefficient in the intima	1	Escuer et al. [2020]
γ_m	Hindrance coefficient in the media	0.845	Escuer et al. [2020]
γ_a	Hindrance coefficient in the adventitia	1	Escuer et al. [2020]
γ_{i_2}	Hindrance coefficient in the plaque	1	Estimated
κ_{ses}	Darcy permeability in the intima	$2.2{\cdot}10^{-16}$ m^2	Ai and Vafai [2006]
κ_m	Darcy permeability in the media	$2{\cdot}10^{-18}$ m^2	Zunino [2004]
κ_a	Darcy permeability in the adventitia	$2{\cdot}10^{-18}$ m^2	Vairo et al. [2010]
κ_{pfc}	Darcy permeability in the fibrous cap	10^{-20} m^2	Ferreira et al. [2018]
κ_{pc}	Darcy permeability in the plaque core (fibrotic)	10^{-20} m^2	Ferreira et al. [2018]
κ_{pc}	Darcy permeability in the plaque core (lipid)	10^{-20} m^2	Ferreira et al. [2018]
κ_{pc}	Darcy permeability in the plaque core (calcified)	0 m^2	Ferreira et al. [2017]
$L_{p,et}$	Hydraulic conductivity of endothelium	$2.2{\cdot}10^{-12}$ m^2 s kg^{-1}	Bozsak et al. [2014]
$L_{p,iel}$	Hydraulic conductivity of IEL	$2.2{\cdot}10^{-9}$ m^2 s kg^{-1}	Bozsak et al. [2014]
$L_{p,eel}$	Hydraulic conductivity of EEL	$2.2{\cdot}10^{-9}$ m^2 s kg^{-1}	Escuer et al. [2020]
C_0	Initial concentration in the polymeric coating	100 mol m^{-3}	Bozsak et al. [2014]
D_c	Effective diffusion coefficient in the coating	10^{-13} m^2 s^{-1}	Mongrain et al. [2005]
D_l	Effective diffusion coefficient in the lumen	$4.1{\cdot}10^{-12}$ m^2 s^{-1}	Bozsak et al. [2014]
D_{ses}	Effective diffusion coefficient in the intima	$1.67{\cdot}10^{-11}$ m^2 s^{-1}	Bozsak et al. [2014]
$D_{m,r}$	Effective radial diffusion coefficient in the media	$7{\cdot}10^{-12}$ m^2 s^{-1}	Levin et al. [2004]
$D_{m,z}$	Effective axial diffusion coefficient in the media	$4{\cdot}10^{-11}$ m^2 s^{-1}	Levin et al. [2004]
D_a	Effective diffusion coefficient in the adventitia	$4{\cdot}10^{-12}$ m^2 s^{-1}	Escuer et al. [2020]
D_{pfc}	Effective diffusion coefficient in the fibrous cap	$6.23{\cdot}10^{-12}$ m^2 s^{-1}	Hossain et al. [2012]
D_{pc}	Effective diffusion coefficient in the plaque core (fibrotic)	$6.23{\cdot}10^{-12}$ m^2 s^{-1}	Hossain et al. [2012]
D_{pc}	Effective diffusion coefficient in the plaque core (lipid)	$6.23{\cdot}10^{-12}$ m^2 s^{-1}	Hossain et al. [2012]
D_{pc}	Effective diffusion coefficient in the plaque core (calcified)	0 m^2 s^{-1}	Ferreira et al. [2017]
P_{et}	Permeability of ET	$3.6{\cdot}10^{-6}$ m s^{-1}	Bozsak et al. [2014]
P_{iel}	Permeability of IEL	$9.6{\cdot}10^{-6}$ m s^{-1}	Bozsak et al. [2014]
P_{eel}	Permeability of EEL	$9.6{\cdot}10^{-6}$ m s^{-1}	Escuer et al. [2020]
s_{et}	Sieving coefficient in the ET	0.855	Bozsak et al. [2014]
s_{iel}	Sieving coefficient in the IEL	1	Bozsak et al. [2014]
s_{eel}	Sieving coefficient in the EEL	1	Escuer et al. [2020]
K_d^{ns}	Non-specific equilibrium dissociation constant	$2.6{\cdot}10^{-3}$ mol m^{-3}	Tzafriri et al. [2009]
k_{on}^{ns}	Non-specific drug binding rate constant	2 m^3 mol^{-1} s^{-1}	Tzafriri et al. [2009]
k_{off}^{ns}	Non-specific drug unbinding rate constant	$5.2{\cdot}10^{-3}$ s^{-1}	McGinty and Pontrelli [2016]
$b_{max,m}^{ns}$	Non-specific binding site density in the media	0.363 mol m^{-3}	Tzafriri et al. [2012]
K_d^s	Specific equilibrium dissociation constant	$2{\cdot}10^{-7}$ mol m^{-3}	Bierer et al. [1990]
k_{on}^s	Specific drug binding rate constant	800 m^3 mol^{-1} s^{-1}	Wear and Walkinshaw [2007]
k_{off}^s	Specific drug unbinding rate constant	$1.6{\cdot}10^{-4}$ s^{-1}	McGinty and Pontrelli [2016]
$b_{max,m}^s$	Specific binding site density in the media	0.0033 mol m^{-3}	Tzafriri et al. [2012]
$b_{max,pfc}$	Total binding site density in the fibrous cap	0.03 mol m^{-3}	Ferreira et al. [2018]
$b_{max,pc}$	Total binding site density in the plaque core (fibrotic)	0.03 mol m^{-3}	Ferreira et al. [2018]
$b_{max,pc}$	Total binding site density in the plaque core (lipid)	0.366 mol m^{-3}	Estimated
$b_{max,pc}$	Total binding site density in the plaque core (calcified)	0 mol m^{-3}	Estimated

Table 3 Summary of the different cases considered in the simulations. In each case, the initial concentration of drug in the polymeric coating of the stent is fixed to 100 mol·m^{-3} [Bozsak et al., 2014].

Case	Radius of curvature (R)	Curvature (κ)	Plaque?
Case 1	∞	0	No
Case 2	60 mm	0.025	No
Case 3	30 mm	0.05	No
Case 4	15 mm	0.1	No
Case 5	7.5 mm	0.2	No
Case 6	3.75 mm	0.4	No
Case 7	15 mm	0.1	Yes (Fibrotic core)
Case 8	15 mm	0.1	Yes (Lipid core)
Case 9	15 mm	0.1	Yes (Calcified core)

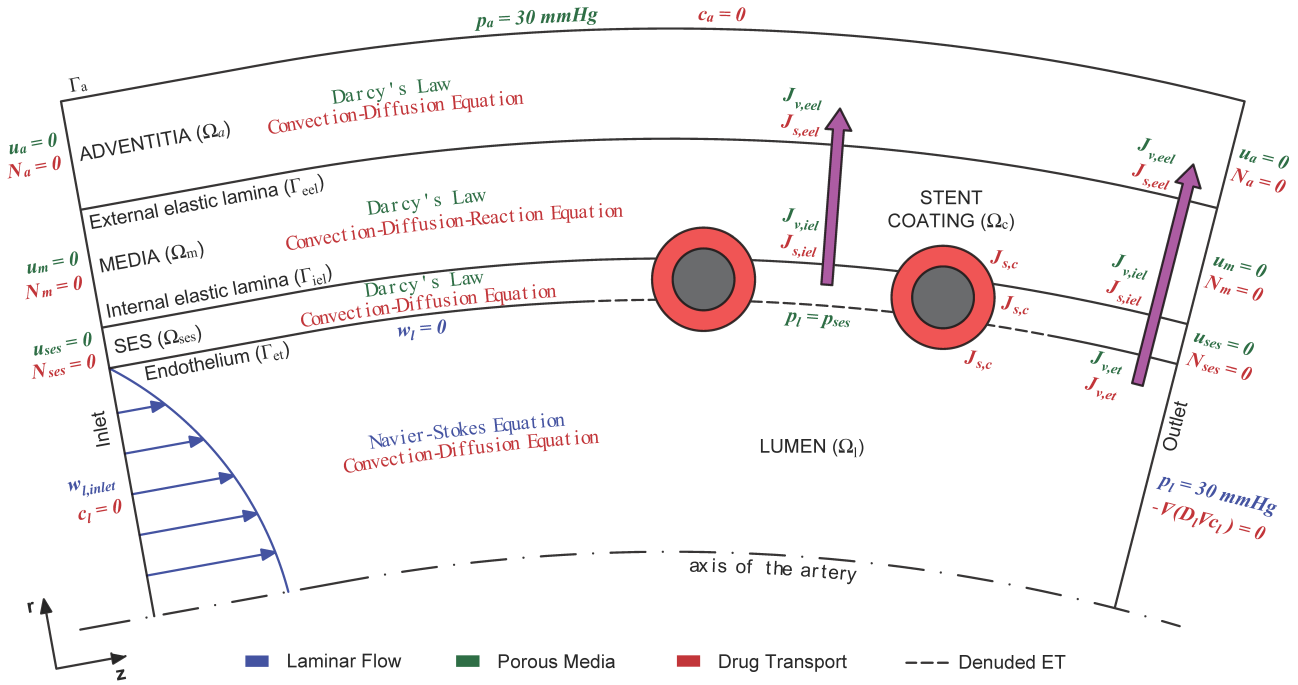

Fig. 1 Schematic summarising the governing equations and the boundary conditions of the computational model.

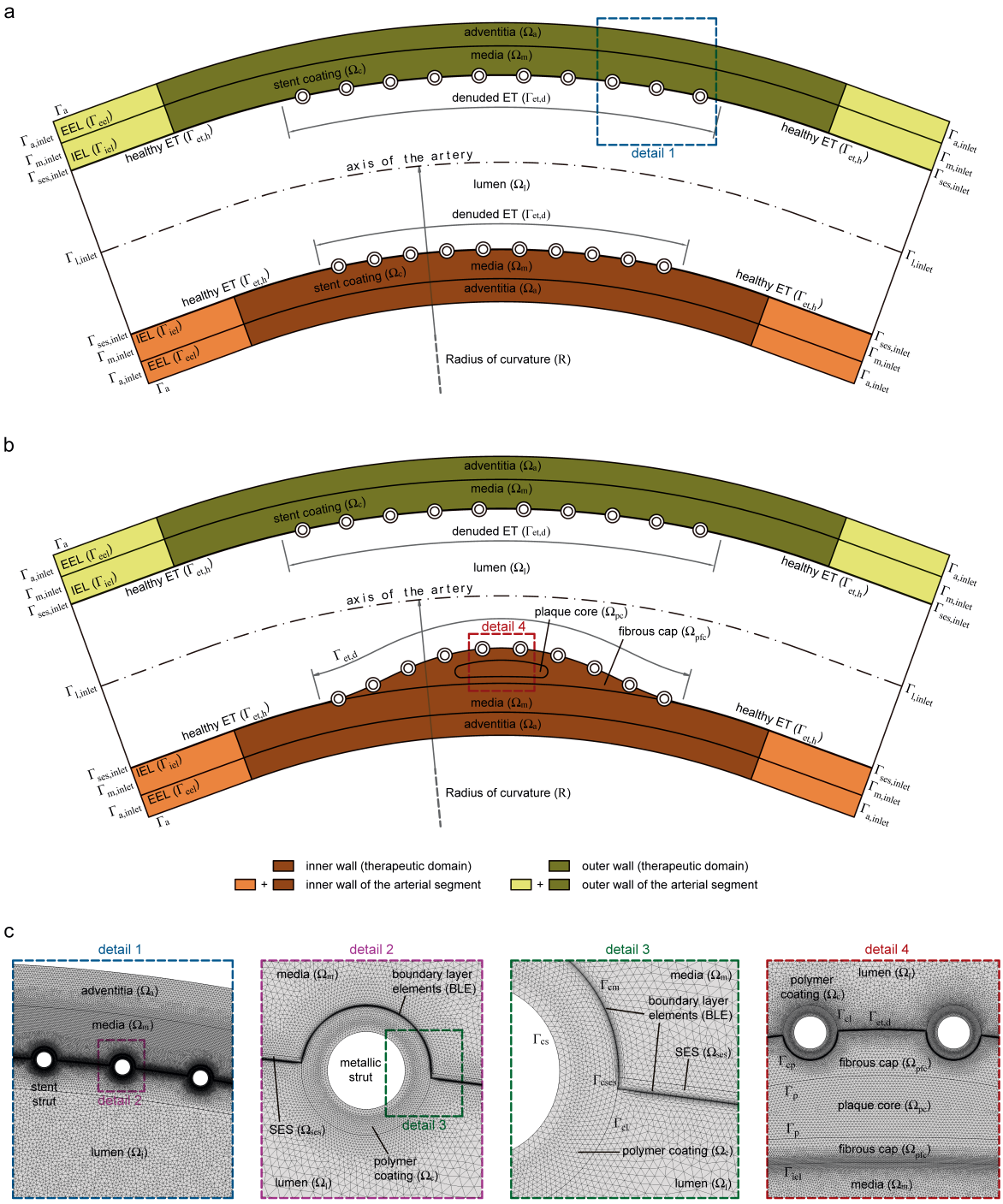

Fig. 2 (a) Overall longitudinal section view of a curved segment of a coronary artery with average curvature ($\kappa = 0.1$) where a DES was implanted. (b) Overall longitudinal section view of a stenosed curved segment of a coronary artery with average curvature ($\kappa = 0.1$ [Jayarama, 2006]) with an atherosclerotic plaque located between the DES and the media. In both cases (healthy and unhealthy) the stent struts are assumed to be half-embedded in the tissue. The target areas for drug transport, also called therapeutic domains, considered to compute all the variables involved in the model are shaded in dark green for the outer wall and in dark brown for the inner wall. These domains are defined as three times the interstrut distance measured in the centerline of the artery (2.1 mm) [Bozsak et al., 2014; Escuer et al., 2020] and then projected radially to each wall. (c) Detailed view of the finite element (FE) mesh used in the computations. As shown in the figure, domains are represented by Ω and boundaries by Γ. Domains are: Ω_l defines the arterial lumen; Ω_{ses} the SES; Ω_m the media layer; Ω_a the adventitia; Ω_{pfc} the fibrous cap of the plaque; Ω_{pc} the plaque core and; Ω_c the polymeric coating of the stent. Boundaries are: Γ_{et} defines the endothelium; Γ_{iel} the internal elastic lamina; Γ_{eel} the external elastic lamina; Γ_a the perivascular side of the vessel; Γ_{cl} the stent coating-lumen interface; Γ_{cses} the coating-SES interface; Γ_{cm} the coating-media interface; Γ_{cs} the coating-metallic strut interface; $\Gamma_{l,inlet}$ and $\Gamma_{l,outlet}$ the inlet and outlet boundaries of the lumen, respectively and; $\Gamma_{i_1,inlet}$ and $\Gamma_{i_1,outlet}$ the inlet and outlet boundaries of the healthy tissue, respectively.

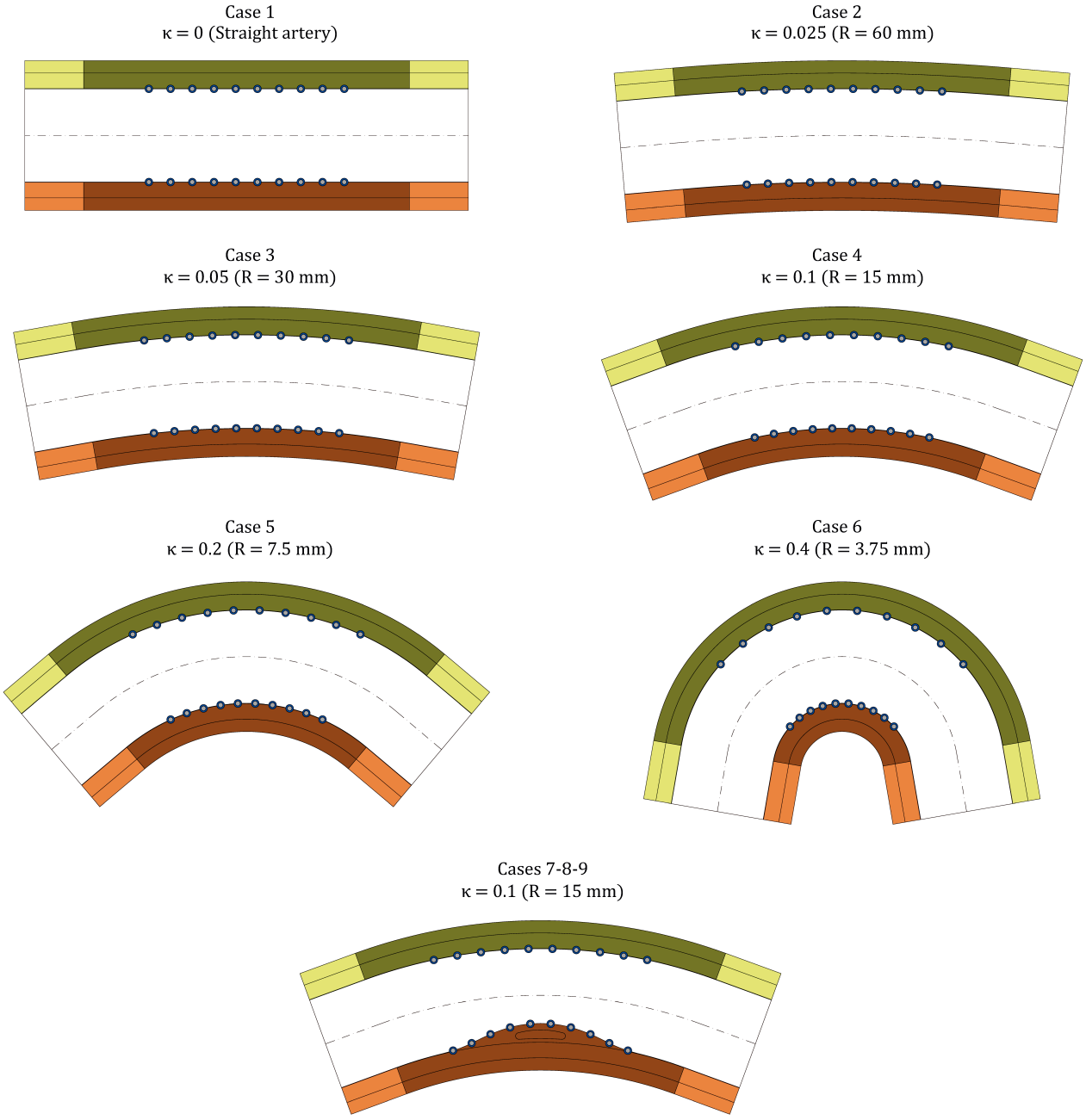

Fig. 3 Schematic showing the geometry of all investigated cases.

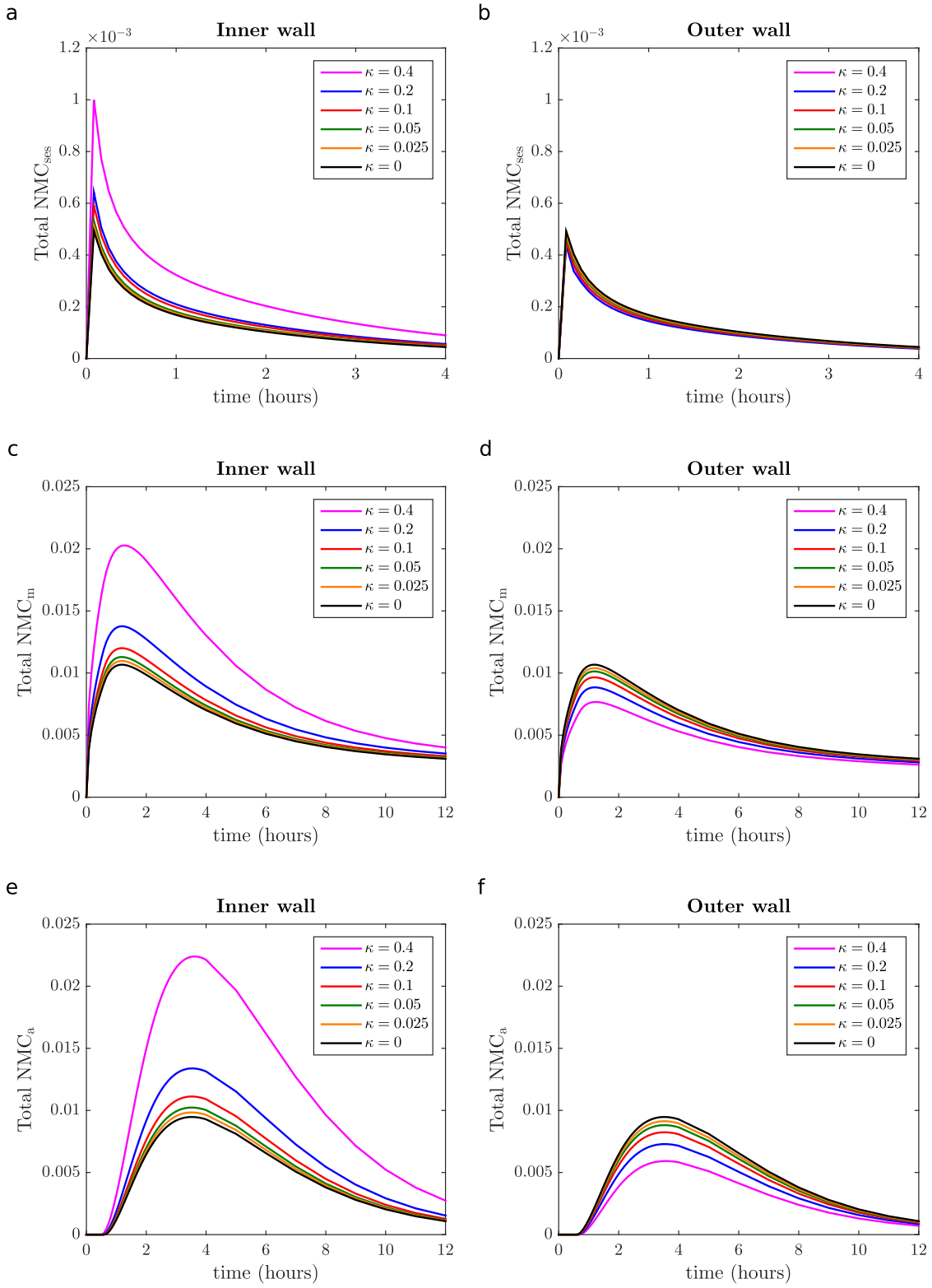

Fig. 4 Time-varying profiles of total normalised mean concentration (NMC) of sirolimus in each layer of the inner and outer wall of the artery: SES (a, b); media (c, d) and adventitia (e, f). The results are shown for the straight model ($\kappa = 0$) and for five different degrees of arterial curvature ($\kappa = 0.025 - 0.4$). Notice that the scales of x- and y-axes for the NMC in the SES (a, b) are different from the rest of the subfigures.

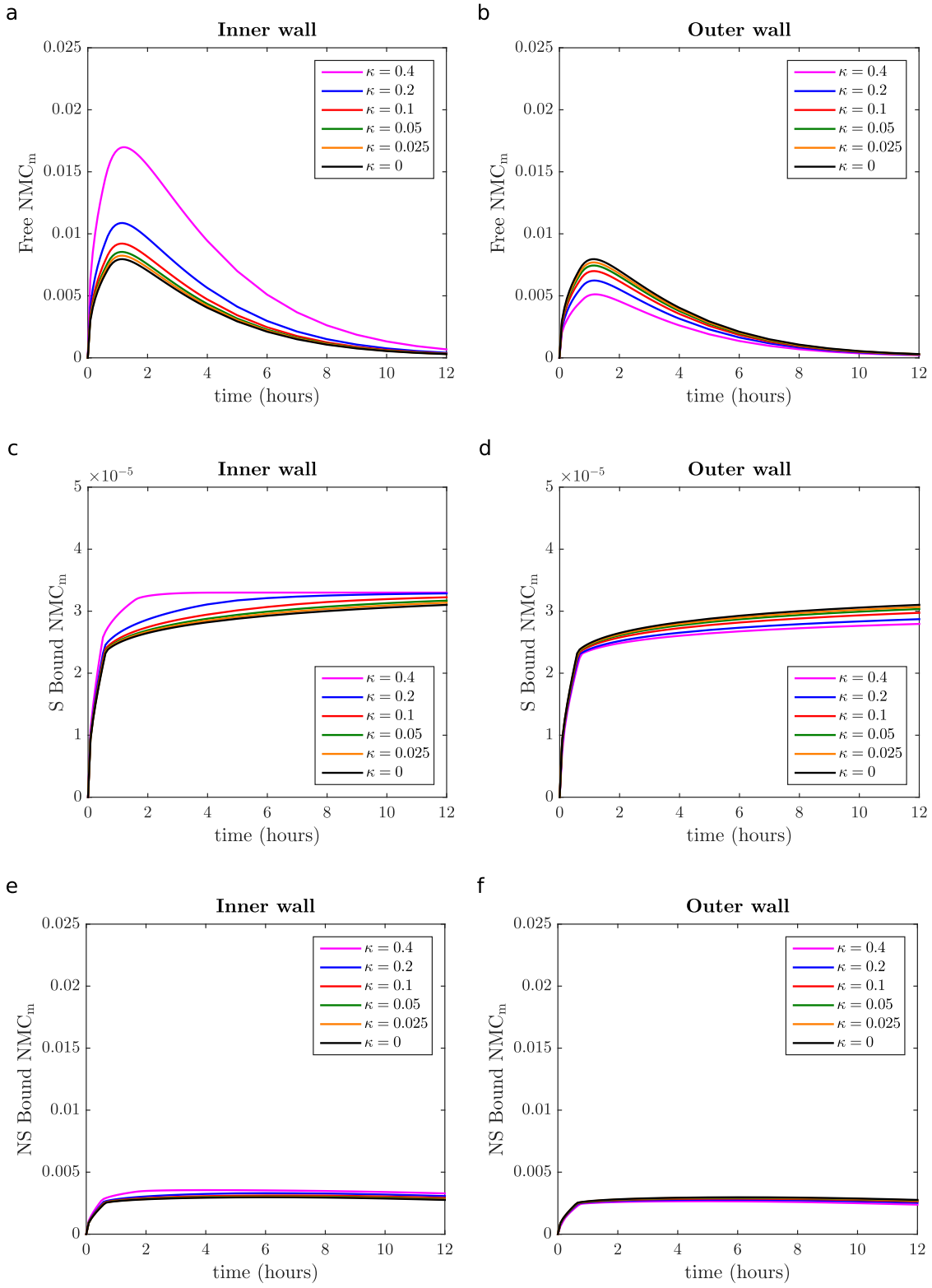

Fig. 5 Time-varying profiles of free NMC (a, b), specific (S) bound NMC (c, d) and non-specific (NS) bound NMC (e, f) of sirolimus in the media layer of the inner and outer wall of the artery, respectively. The results are shown for the straight model ($\kappa = 0$) and for five different degrees of arterial curvature ($\kappa = 0.025 - 0.4$). Notice that the scales of y-axes for the specific (S) bound NMC (c, d) are different from the rest of the subfigures.

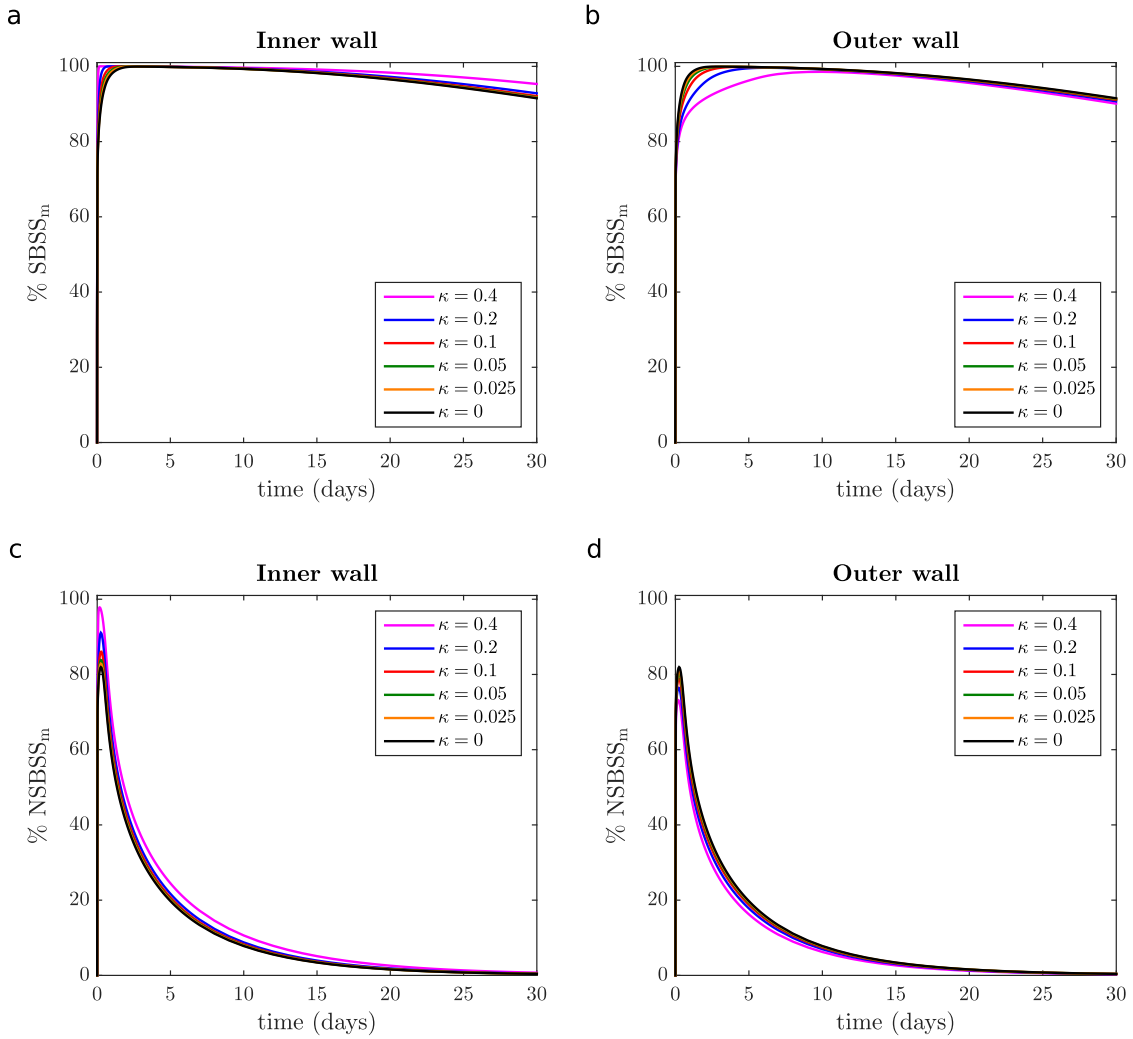

Fig. 6 Specific (target receptor) and non-specific (ECM) binding site % saturation in the media layer of the inner and outer wall of the artery as a function of time, respectively. The results are shown for the straight model ($\kappa = 0$) and for five different degrees of arterial curvature ($\kappa = 0.025 - 0.4$).

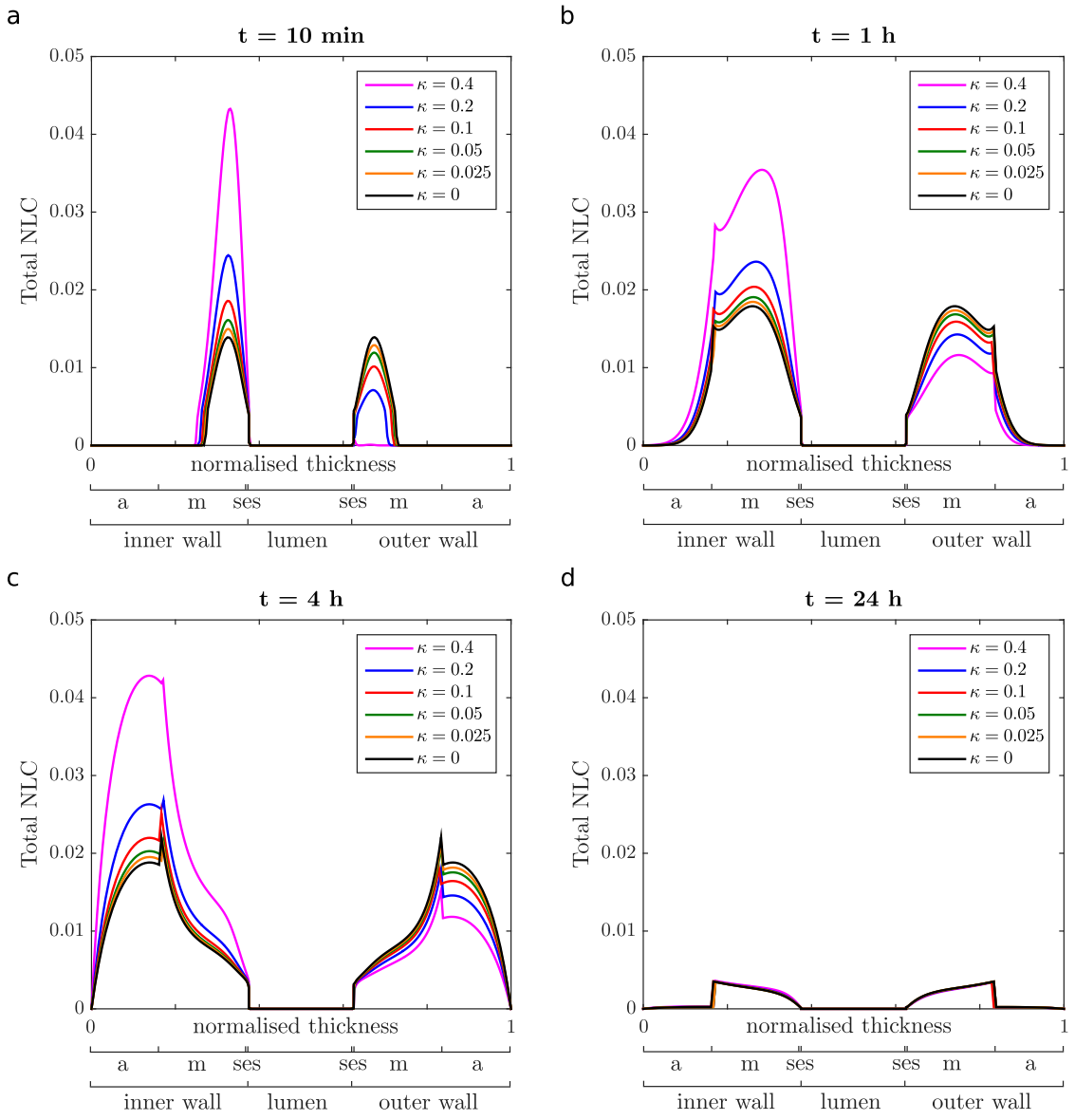

Fig. 7 Spatially varying profiles of total normalised local concentration (NLC) of sirolimus in the tissue, calculated as $(c_i+b_i^s+b_i^{ns})/C_0$, at 10 min (a), 1 hour (b), 4 hours (c) and 1 day (d) after stent implantation. The results are shown for the straight model ($\kappa = 0$) and for five different degrees of arterial curvature ($\kappa = 0.025 - 0.4$) in a radial section between the middle stent struts. Note that lumen diameter is not drawn to scale.

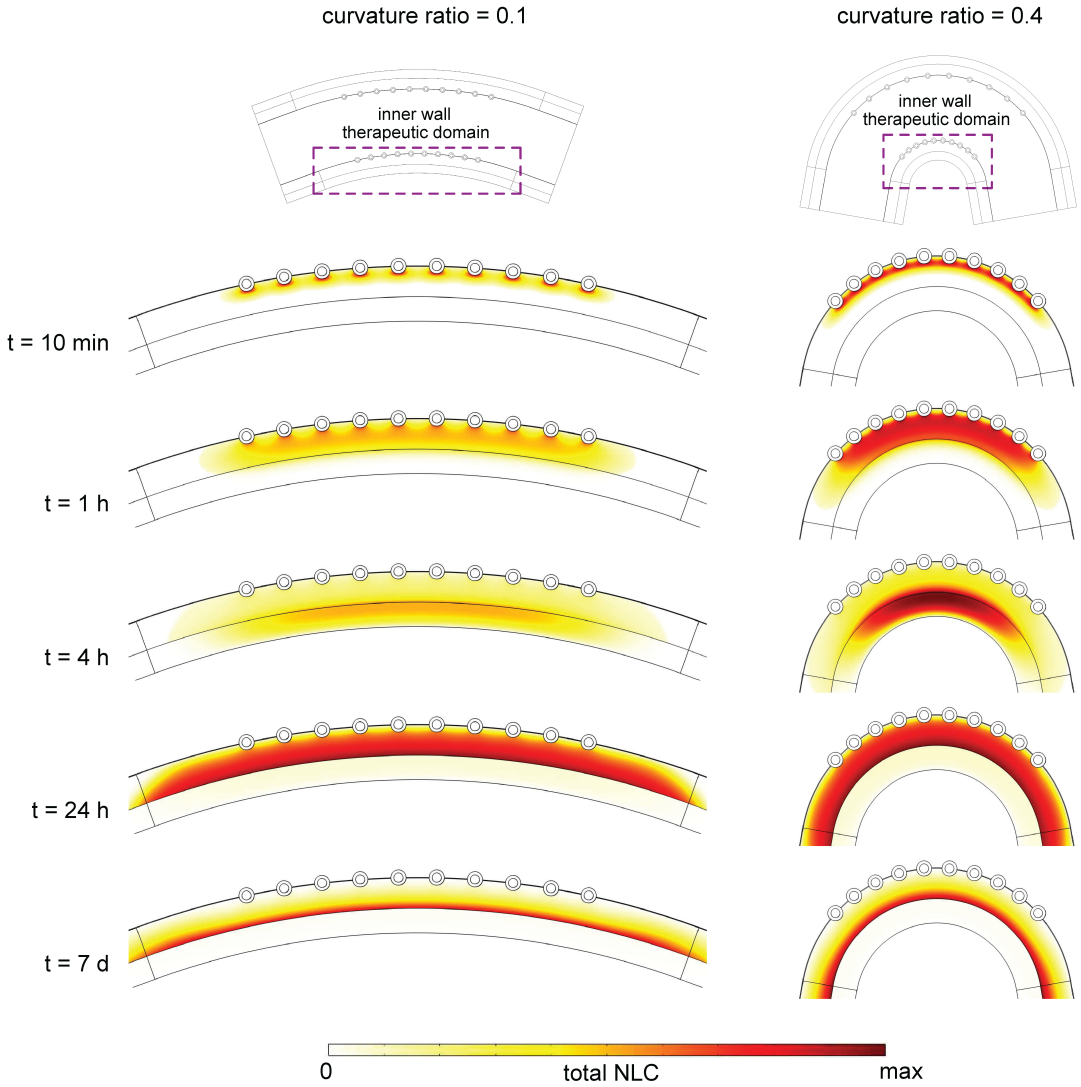

Fig. 8 Spatial variation of total NLC of sirolimus, calculated as $(c_i + b_i^s + b_i^{ns})/C_0$, within the inner wall of the artery at five different time points (t = 10 min , t = 1 hour, t = 4 hours, t = 24 hours and t = 7 days) for curvature ratios of $\kappa = 0.1$ (average curvature ratio) and $\kappa = 0.4$, respectively. For each time point the same colour scale is used for both cases of curvature. The maximum values of total NLC of drug chosen for each time point are the following: max = $6.23 \cdot 10^{-2}$ at t = 10 min; max = $4.16 \cdot 10^{-2}$ at t = 1 h; max = $4.56 \cdot 10^{-2}$ at t = 4 h; max = $3.65 \cdot 10^{-3}$ at t = 24 h and; max = $1.74 \cdot 10^{-3}$ at t = 7 d. Tables with the maximum values at each time point may be found in Section S4 of the Supplementary Material.

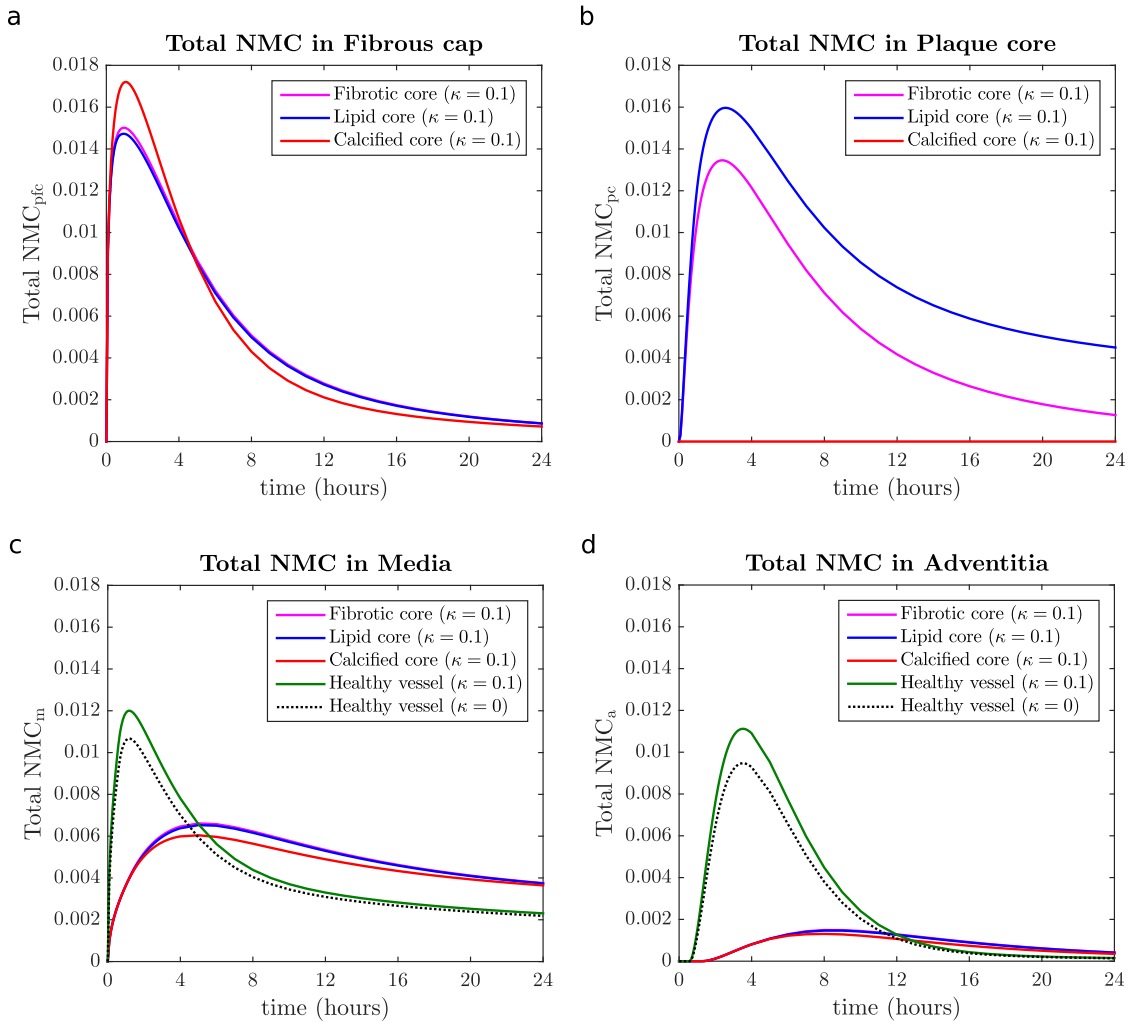

Fig. 9 Time-varying profiles of the total NMC of sirolimus in the fibrous cap (a), plaque core (b), media (c) and adventitia (d) within the inner wall of the artery for a curvature ratio of $\kappa = 0.1$ (average curvature ratio). The results are shown for three different plaque core compositions: fibrotic, lipid and calcified. In case of the media and adventitia, the results are also shown for the straight model ($\kappa = 0$) and for a curvature ratio of $\kappa = 0.1$, both under healthy conditions (i.e. healthy vessel without plaque).

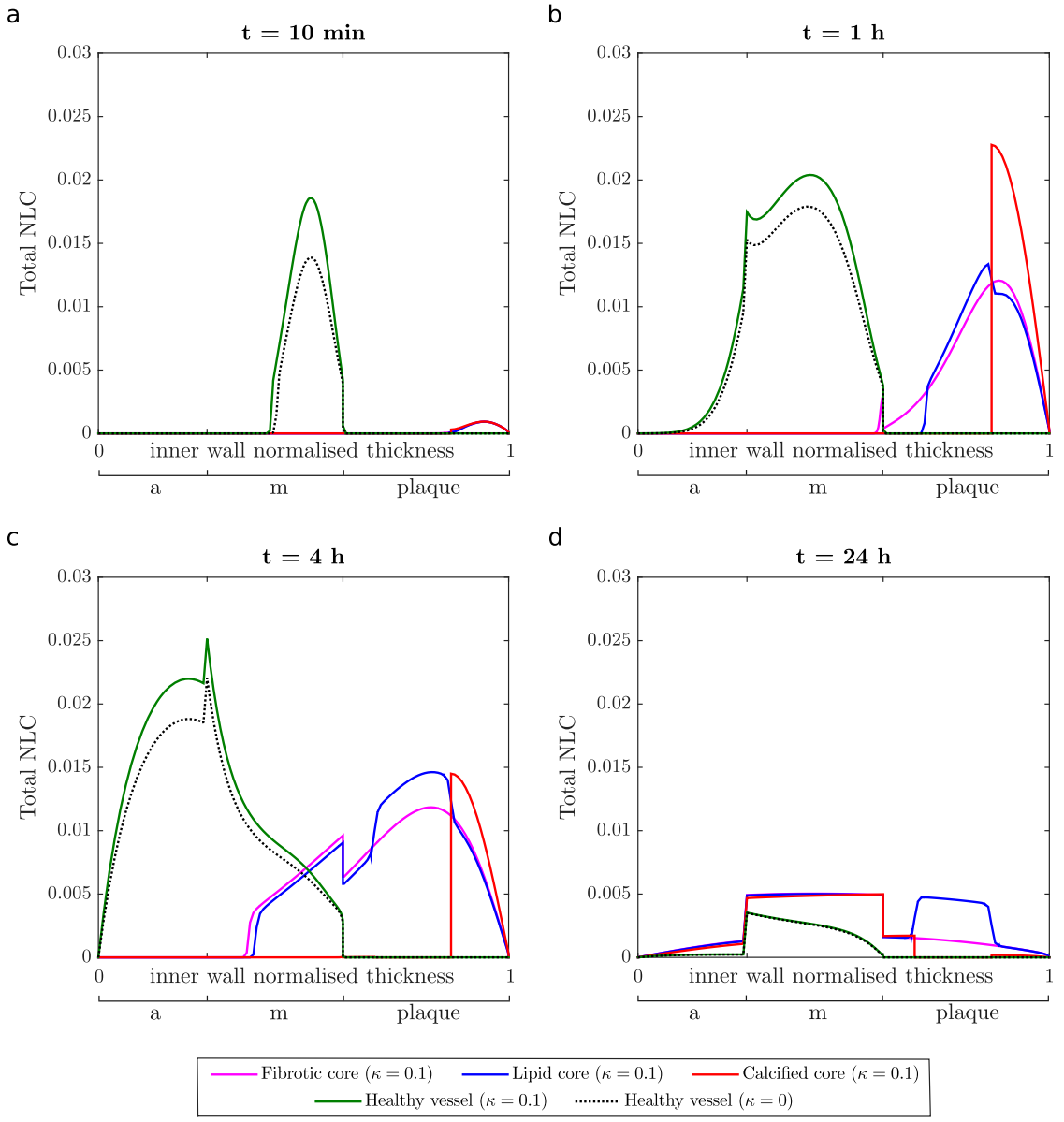

Fig. 10 Spatially varying profiles of total NLC of sirolimus, calculated as $(c_i + b_i^s + b_i^{ns})/C_0$, in the inner wall of the artery at 10 min (a), 1 hour (b), 4 hours (c) and 1 day (d) after stent implantation in a radial section between the middle stent struts. The results are shown for three different plaque core compositions: fibrotic, lipid and calcified for a curvature ratio of $\kappa = 0.1$ (average curvature ratio). Moreover, the results for the straight model ($\kappa = 0$) and for a curvature ratio of $\kappa = 0.1$, both under healthy conditions (i.e. healthy vessel without plaque) are shown.